



Numerical modeling of borehole breakouts formation in various stress fields using a Higher-Order Displacement Discontinuity Method (HODDM)

Abolfazl Abdollahipour ¹; Mohammad Fatehi Marji ^{2*}

1. School of Mining Engineering, College of Engineering, University of Tehran, Tehran, Iran
2. Faculty of Mining and Metallurgical Engineering, Yazd University, Yazd, Iran

Received: 07 June 2021; Accepted: 12 January 2022

DOI: 10.22107/jpg.2022.289572.1139

Keywords

Borehole Breakout
Wellbore stability
Indirect BEM
Crack propagation
Fracture mechanics

Abstract

Borehole breakouts can be modeled by the propagation of cracks in the vicinity of wellbores. Coalescence of these cracks with a series of formed sub-parallel cracks leads to a breakout. Using fracture mechanics principles, the propagation of cracks in the vicinity of wellbores resulting in the final formation of breakouts is investigated. An indirect BEM with higher-order elements has been used to numerically simulate cracks propagation. Various configurations of cracks placement around a wellbore are analyzed. Numerical results showed that the ratio of stresses normal to wellbores' axis has a significant effect on breakouts final shape. For a given lower normal stress, higher stress ratios lead to wider breakouts, eventually leading to wellbore instability. Furthermore, for a given higher normal stress, higher stress ratios tend to form deeper breakouts with a limited width increase. The hydrostatic stress field can be completely stable or unstable depending on a threshold stress value.

1. Introduction

Wellbore breakouts occur due to compressive stress concentration around wellbores in direction of minimum normal stress to the wellbore wall (minimum horizontal stress in case of vertical wellbores). Many studies have proven that breakouts' orientations are independent of lithology and are uniform with depth (Castillo and Zoback, 1994; Plumb and Cox, 1987). Breakouts result in an elongation of the wellbore wall. They are very common in oil and gas wells and they can be used to estimate stress orientation and magnitude (Zoback, 2010). However, excessive wellbore breakout can lead to wellbore instability. Breakouts and related problems in wellbore

stability have been extensively studied using analytical and numerical models and field data (Gerolymatou, 2019a; Gomar et al., 2014; Li et al., 2019; Lin et al., 2010; Mansouri Zadeh et al., 2016; Sahara et al., 2017; Zhang et al., 2018). Gerolymatou suggested a semi-analytical method based on conformal mapping for the prediction of breakouts in brittle rock (Gerolymatou, 2019b). Lin et al. and Liu et al. used DEM to simulate breakout formation. They showed that breakout shape and dimensions changed considerably under high stress and high temperature conditions (Lin et al., 2020; Liu et al., 2020). Wei et al. developed a hydro-mechanical model for

borehole breakout in fractured rocks. They showed that the fracture density dominates the yielded area around the borehole, while the direction of the fractures controls the shape of the breakout (Wei et al., 2021). Tang et al. used a thermo-poroelasticity model to analyze wellbore breakout and determine maximum horizontal stress (Tang et al., 2021). As wellbore breakouts grow, they deepen but do not widen (Zoback, 2010). Therefore, a wellbore with a limited breakouts' width can be considered stable.

Studies of wellbore breakouts have shown that failure of wellbore walls is often dominated by a tensile spalling or shear fracturing mode (Guenot, 1989; Vardoulakis et al., 1988). Various studies have focused on these two breakout mechanisms. Tensile crack initiation and propagation in the vicinity of wellbore results in tensile spalling. Coalescence of these tensile cracks with a series of formed sub-parallel cracks creates a tensile spalling layer (Baotang et al., 2014). This is typical behavior of hard crystalline rocks such as granites (Amadei and Stephansson, 1997; Ewy and Cook, 1990; Haim son and Lee, 1995; Lee and Haim son, 1993; Martin et al., 1994; Zang and Stephansson, 2010). Also, the extension of shear failure along with one or more shear fractures from the wellbore wall into the rock results in shear fracturing. The intersection of these shear fractures can cause breakouts. The shear fracturing mechanism of breakout formation is often observed in softer porous rocks, such as dolomite, limestone, and sandstone (Guenot, 1989; Zoback et al., 1985). Fracture mechanics concepts have been used to study breakout formation. Shen et al. (Shen et al., 2002) and Shen (Shen, 2008) used FRACOD (based on fracture mechanics principles) to estimate in situ stress magnitudes from breakouts. Abdollahipour et al. also used fracture mechanics concepts and the displacement discontinuity method (DDM) to study hydraulically induced fracture propagation around wellbores (Abdollahipour, 2015; Abdollahipour et al., 2015, 2013). They also improved the DDM by extending it to

Poroelasticity (A Abdollahipour et al., 2016).

In this study, fracture mechanics concepts along with the DDM were used to study breakout formation in various conditions. First, the numerical method was introduced and verified. Then, a series of numerical simulations were carried out and to study breakout formations in various conditions.

2. Research Methodology

The displacement discontinuity method (DDM) is particularly ideal for problems involving fractures and discontinuities because the fundamental solution contains a displacement jump. Therefore, normal displacement discontinuities of the element can be considered as the normal displacements of a crack and its shear displacement discontinuities can be considered as shear displacements of a crack. A 2D displacement discontinuity method has been used for numerical analyses. The rock mass is assumed to be impermeable and uniform pressure of 5 MPa is considered in wellbores as the mud pressure. Following properties (based on field data (RIPI, 2016)) and assumptions have been also considered through analyses unless told otherwise. Wellbore axis with radius R is aligned with vertical stress which is one of the principal stresses. Special crack tip elements (as explained in section 3.2) were used for cracks' ends to simulate cracks propagation more accurately. Maximum and minimum horizontal stresses vary in a domain as $\sigma_H=(40-80\text{MPa})$ and $\sigma_h=(10-40\text{MPa})$ respectively. Two initial geometries of circular cracks (Fig. 1 (a)) with distance r from the wellbore wall and random cracks (Fig. 1(b)) are considered in this study.

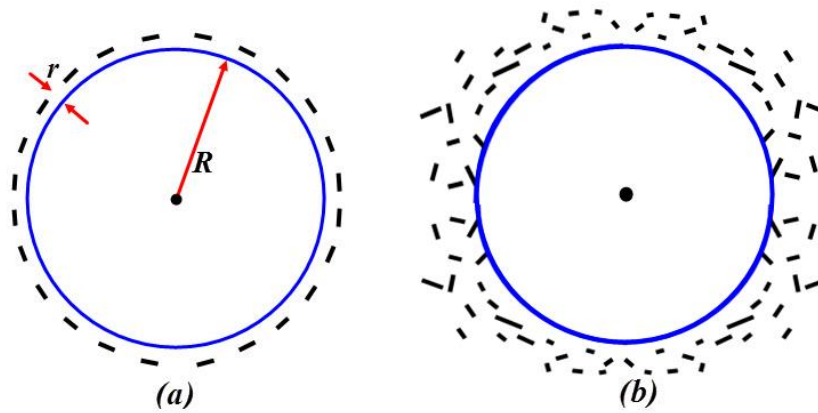


Figure. 1 Initial geometry of cracks around a wellbore

Table 1 presents the geomechanical properties considered in the analyses based on laboratory tests on oilfield specimens. Where E is the

modulus of elasticity, ν is the Poisson ‘s ratio, and UCS is the uniaxial compressive strength.

Table 1. Geomechanical properties

$E(GPa)$	$UCS (MPa)$	$K_{IC} (MPa \cdot \sqrt{m})$	ν
35	115	3.5	0.28

The crack initiation angle of propagating cracks θ_0 is determined based on the maximum tangential stress mixed-mode fracture criterion proposed by Erdogan and Sih (Erdogan and Sih, 1963).

The initial cracks may propagate in the numerical models according to the following steps.

- 1) The model is run,
- 2) Crack initiation angle θ is determined based on the maximum tangential stress criterion, for propagating cracks in the model.
- 3) Special crack tip elements of the propagated cracks are converted to ordinary 3rd order elements.
- 4) A special crack tip element with a length of $0.1L$ (i.e., one-tenth of initial cracks) is added in the direction of θ_0 .

The numerical model repeats these 4 steps until all cracks are interacted and stop propagating

and the final shape of crack propagation leading to breakout formation is formed or no more crack propagation is observed based on the fracture criterion.

3. Higher-order displacement discontinuity method

Higher-order elements increase the accuracy of the displacement discontinuity method. Third-order elements of displacement discontinuity were used in this study for higher accuracy. However, due to singularity in the vicinity of crack tips, the accuracy of the DDM decreases. The use of special crack tip elements at the end of cracks increases the accuracy and overcomes the lack of accuracy near crack tips. Therefore, a special crack tip element with four sub-elements was also used to further increase the accuracy of the DDM. Appendix A provides the complete set of equations for the

formulation of the used numerical model.

4. Verification of the third-order element formulation of the DDM

The accuracy and applicability of the third-order element DDM (i.e., cubic elements) are tested against problems of a slant crack in an infinite body and cracks emanating from a circular hole (which both have analytical solutions for Mode I and II SIFs).

Crack in an infinite body

A slant crack in an infinite body under uniform tension is shown in Fig. 2(a). Guo et al. and Whittaker et al. calculated the analytical KI and KII for this problem (Guo et al., 1990; Whittaker et al., 1992). A crack half-length of $a=1\text{ m}$ is assumed in the analysis. A crack tip element length to half crack length ratio, $l/a=0.1$ has been used for the numerical solution of the problem.

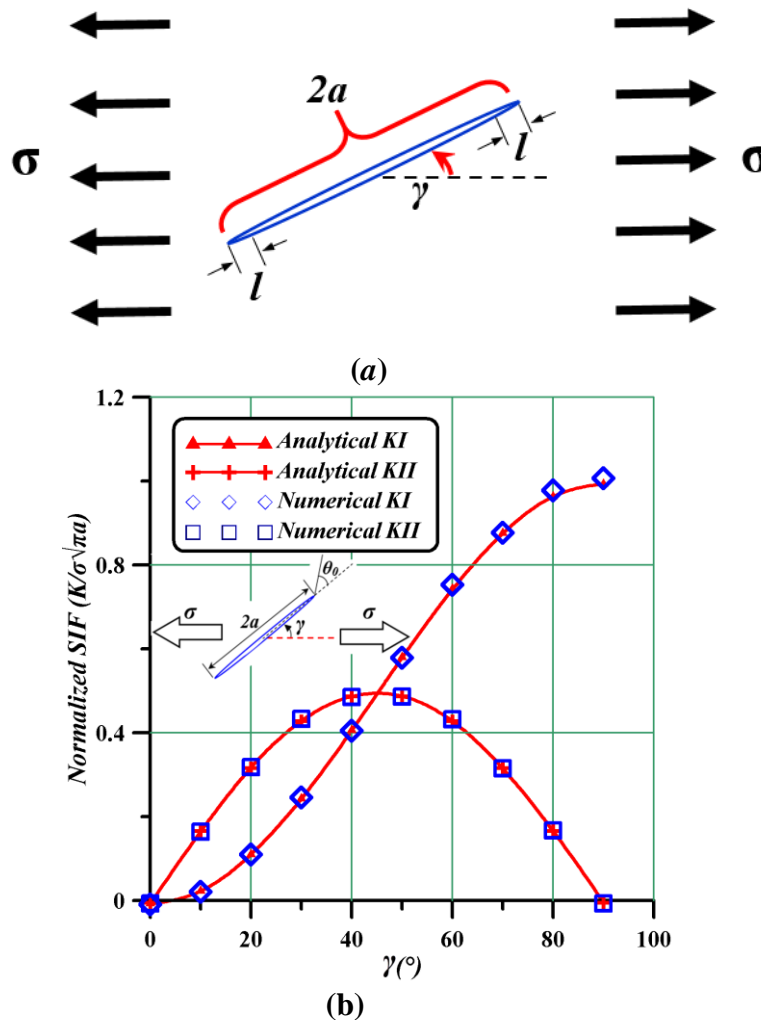


Figure. 2. (a) Crack geometry (b) comparison of normalized SIFs for a slant crack in an infinite body with arbitrary orientation (b) compares the numerical and analytical values for the normalized SIFs. The numerical method has successfully predicted Mode I and II SIFs for various inclinations angles of the crack.

$$K_I = \sigma \sqrt{\pi a} \sin^2 \gamma \quad \text{and} \quad K_{II} = \sigma \sqrt{\pi a} \sin \gamma \cos \gamma \quad (15)$$

Cracks emanating from a circular hole

Fig. 3 shows two cracks emanating from a circular hole both under uniform internal pressure P . Newman (Newman, 1971) and Tada et al. (Tada et al., 2000) provided the analytical solution for the calculation of mode I stress intensity factor of this problem. The geometry of the problem is very similar to that of a wellbore with perforations. It is solved numerically to verify the accuracy of the

proposed third-order formulation. Various crack lengths (a) have been used along with the values shown in Fig. 3. Fig. 4 shows K_I values for various cracks' lengths. The comparison shows the high accuracy of the method in predicting Mode I SIF. Since the problem is very similar to the geometry of a borehole with cracks on the wellbore's wall, it also implies a high level of accurate simulation of SIF calculation around a wellbore.

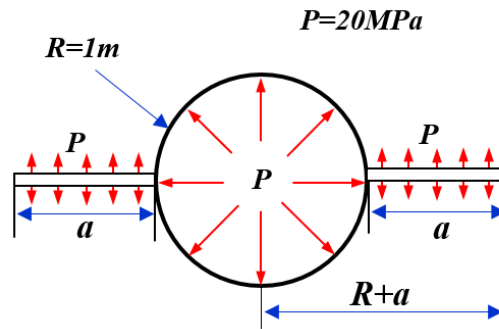


Figure 3. Cracks emanating from a circular hole with radius R and internal pressure P

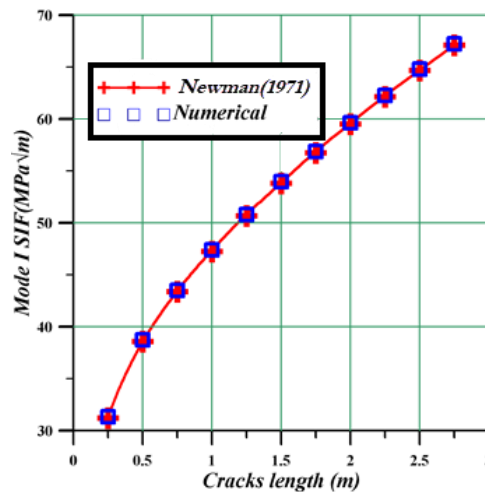


Figure 4. Comparison of numerical and analytical K_I values for cracks emanating from a circular hole

5. Numerical modeling of breakout formation in various stress fields

The area close to the wellbore wall often contains either natural cracks or induced cracks by a damaged zone around the wellbore (Zoback, 2010). These natural or induced pre-existing cracks may propagate to form breakouts based on the acting stresses on their surfaces and the geomechanical properties of

$$\alpha = \cos^{-1} \left(\frac{1 - (\sigma_H + \sigma_h) / \sigma_c}{2(\sigma_H - \sigma_h) / \sigma_c} \right) \quad (16)$$

where α is breakout angle at the wellbore wall ($^\circ$), σ_c is the uniaxial compressive strength of the rock (MPa), and σ_H and σ_h are maximum and minimum horizontal stresses respectively. Minimum horizontal stress acting in the x-axis direction was varied from 10 to 40 MPa with 10 MPa intervals, while maximum horizontal stress acting in the y-axis direction was varied from 40 to 70 MPa with also 10 MPa intervals. The wellbore radius was $R=0.5\text{m}$ with no internal pressure and cracks are within 5 cm of the wellbore periphery (i.e. $r=5\text{ cm}$). Fig. 5 shows the formation of breakouts around these wellbores while considering the initial geometry shown in Fig. 1 (a). A maximum DDM element length of 5 cm is used throughout the modeling.

It should be noted that Fig. 5 is redrawn manually from the obtained results of numerical modeling. Fig. 5 (a) shows the most crack propagation around wellbores. Due to a relatively low σ_h (=10 MPa), a high difference between the minimum and maximum horizontal stresses has occurred leading to the formation of a compressive and tensile region around the wellbore. Although many initial cracks have propagated in Fig. 5(a), except for the last case, they do not contribute to breakout formations. In fact, the combination of $\sigma_H=40$ MPa with other minimum horizontal stresses didn't produce any significant crack propagation, hence these graphs are not shown.

the host rock. Therefore, the formation of breakouts would be mostly dominated by stress concentrations and the host rock properties .

The Kirsch solution can be used to determine the tangential stress at the wellbore wall based on the elasticity theory. Using Kirsch solution and uniaxial compressive strength of the host rock, one can determine the breakout angle in a vertical wellbore (Baotang et al., 2014) from Eq. (16).

Results are in complete agreement with Eq. (16) which predicts breakout angle $\alpha=0^\circ$ for the omitted cases. Most crack propagations in Fig. 5 (a) are drilling-induced fractures due to the creation of a tension area in specified locations shown by an ellipse on the wellbore walls. This can be easily derived from the Kirsch solution for the developed tangential stresses in the wellbore wall. These cracks can be distinguished from “breakout cracks” by considering that they are deepening instead of spalling and going around the wellbore wall. By increasing the minimum horizontal stress in subsequent analyses, more breakouts were observed (Fig. 5 (b) to (d)). Also, higher stress ratios in subsequent models produced higher breakout angles. It should be noted that breakouts need an initial stress threshold to form. This is why the high-stress ratio of 4 (Fig. 5 (a)) could not form any breakout (due to not reaching this threshold). The threshold can be estimated based on the uniaxial compressive strength of the host rock. According to Fig. 5, the ratio of in situ stresses significantly alters breakout formation and crack propagation path. In the next section, a systematic study of the stress ratio effect on crack propagation will be performed

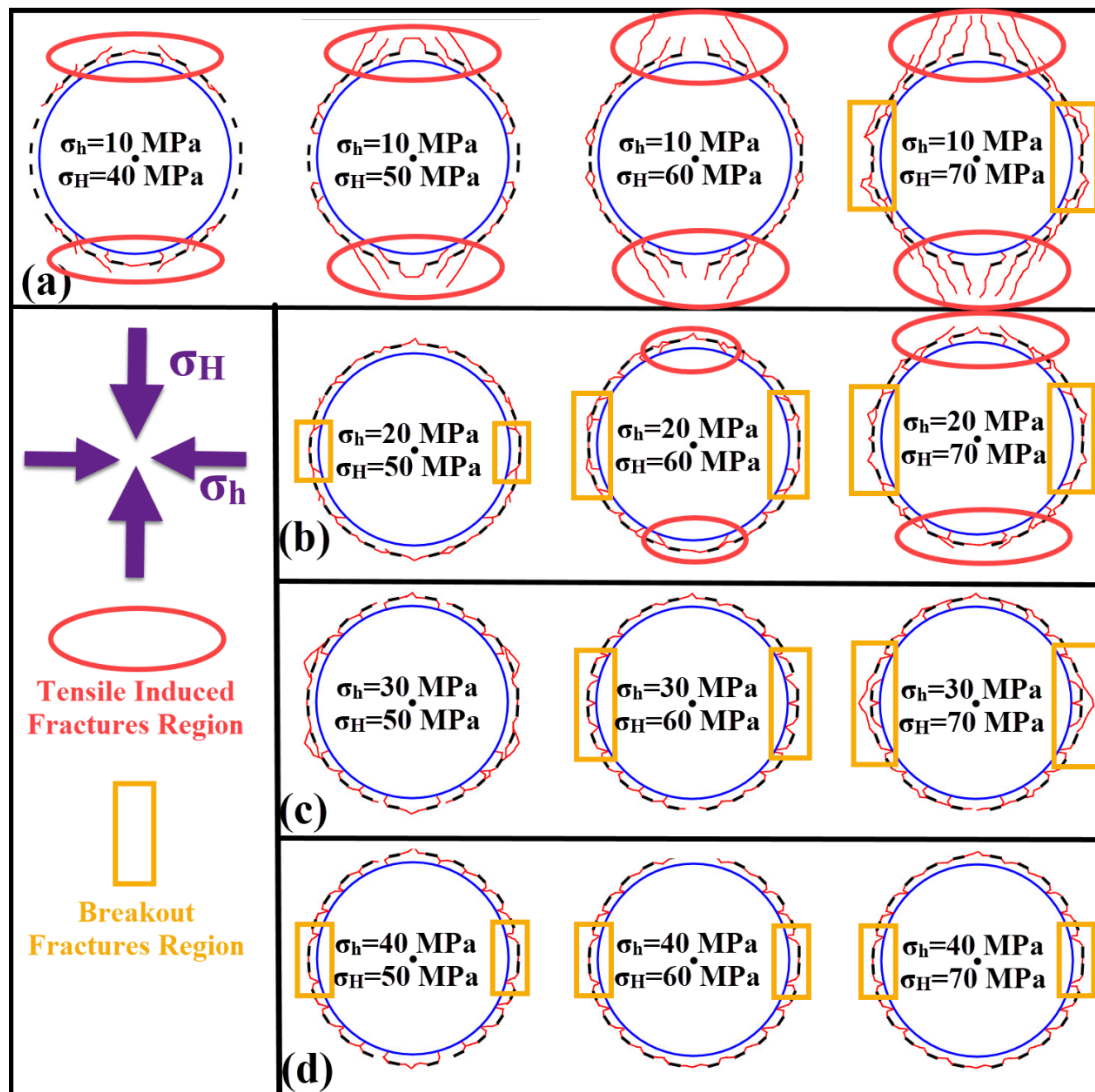


Figure 5. Breakout formation around wellbores with various stress ratios, a) $\sigma_h=10\text{MPa}$, $\sigma_H=40$ to 70 MPa, b) $\sigma_h=20\text{MPa}$, $\sigma_H=50$ to 70 MPa, c) $\sigma_h=30\text{MPa}$, $\sigma_H=50$ to 70 MPa, d) $\sigma_h=40\text{MPa}$, $\sigma_H=50$ to 70 MPa

6. Effect of stress ratio on breakout formation

The ratio of stresses perpendicular to the wellbore wall is known to have a significant effect on the stability of wellbores as well as the concentration of stresses near wellbores. This effect is studied by constructing several models with different stress ratios. Stress ratios (σ_H/σ_h) of 1, 1.5, 2, 3, and 4 with $\sigma_H=70$ MPa along with mud pressure of $P=5$ MPa are

considered. It should be noted that the mud pressure did not affect breakout shape significantly in previous models, hence it is kept constant in all subsequent analyses. Fig. 6 shows the formation of breakouts in these models. The breakout angle is almost similar in all stress ratios in Fig. 7. For ratios of 3 and 4 breakouts have deepened more than it has widened. This limits the collapsed wall due to breakout. This limited breakout width does not

create significant wellbore stability problems. Based on previous experiences wellbores with breakouts width angle (see α in Fig. 6) less than 90° can be considered stable (Zoback, 2010). The maximum horizontal stress is constant in Fig. 6 and minimum horizontal stress is varied to produce different stress ratios. For a stress ratio of 1 (i.e. lithostatic stress state), all cracks have intersected each other around the wellbore. Since in this case, the tangential stress is constant around the wellbore, the crack propagation paths have not changed around the wellbore and a uniform breakout has merged in all the walls. However, the breakout angle for other cases is limited and almost equal, only the depth of breakout has changed in these models. In Fig. 7 minimum horizontal stress is

constant and maximum horizontal stress is changed. For ratios of 1 and 1.5 no significant crack propagation was observed, therefore no breakout was formed. This was expected since the combination of stresses around this well was not high enough to create any considerable failure. The hydrostatic stress state has shown two very different behavior in Figs. 8 and 9. This further suggests threshold stress for initiation of breakout formation. By the increase of stress ratio in Fig. 7, higher stresses act on the wellbore resulting in the initiation of breakout formation at a stress ratio of 2. The changes of stress ratio in other models of Fig. 7 shows that breakout tends to widen as the stress ratio increases.

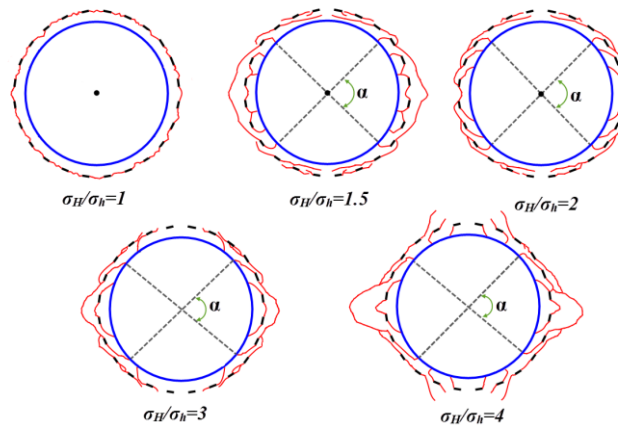


Figure 6. Breakout angle for various stress ratios with $\sigma_H=70$ MPa

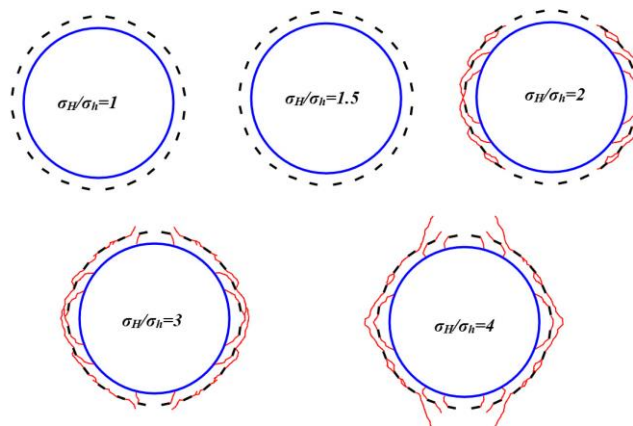


Figure 7. Breakout angle for various stress ratios with $\sigma_h=30$ MPa

Based on Figs. 6 and 7 it can be deduced that for a constant maximum normal stress to wellbore wall, higher stress ratios (maximum to minimum stresses normal to wellbore) results in deeper breakouts with an almost contained width. On the other hand, for a constant minimum normal stress to the wellbore wall, higher stress ratios lead to wider stress ratios, and meanwhile, the depth of breakouts does not change substantially. Also, it can be concluded that the maximum normal stress to the wellbore controls the width of breakout while the depth of breakout is more related to the minimum horizontal stress. Moreover, the hydrostatic stress state (i.e. stress ratio of 1) showed the most breakout formation angle for Fig. 6 and no breakout angle for Fig. 7. This contradicting result may be justified by considering the threshold stress needed for the initiation of crack propagation. These results were obtained considering the initial geometry shown in Fig. 1 (a). A different geometry consisting of random cracks will be considered to examine the findings and evaluate the effect of the initial distribution of initial cracks. Initial cracks with random orientations and lengths are distributed around wellbores as shown in Fig. 8 (a). Figs. 8 (b) to (f) show the breakout formations for $\sigma_H=70$ MPa and σ_H/σ_h ratio of 1, 1.5, 2, 3, and 4 respectively. The extent of breakout formation is still similar to Fig. 6. Again, the stress ratio of 1 shows an almost uniform breakout formation around the wellbore. However, the deepening effect of higher stress

ratios (for a constant maximum normal stress) is clearer in this case. It should be noted that the crack propagation in specified areas of Fig. 8 (e) and (f) is due to the formation of a tensile stress region. This can be seen in Fig. 9 which shows the variation of total displacements around wellbores. Maximum horizontal stress i.e. σ_H is held constant and various ratios of stresses are developed in Fig. 9 (a) while the minimum horizontal stress i.e. σ_h is held constant and various ratios of stresses are developed in Fig. 9 (b). The displacements around the wellbore for stress ratio of 1 are constant and larger than other stress ratios in the majority of the wellbore periphery for $\sigma_H=70$ MPa in Fig. 9 (a). On the other hand, it is smaller than other stress ratios in the majority of the wellbore for $\sigma_h=30$ MPa in Fig. 9 (b). The crack propagations in specified areas of Figs. 8 (e) and (f) are due to tensile stress and they do not contribute to breakout formation since they tend to propagate in a direction normal to minimum horizontal stress. This leads to no cracks intersection which is essential to breakout formation. The results in Figs. 8-11 show that hydrostatic stress states can have two different behaviors. If the hydrostatic stress state produces high enough stresses around the wellbore, it can be one of the most unstable cases. While, if the hydrostatic stress state is not considerably high (in relation to UCS), then it can be one of the most stable stress states.

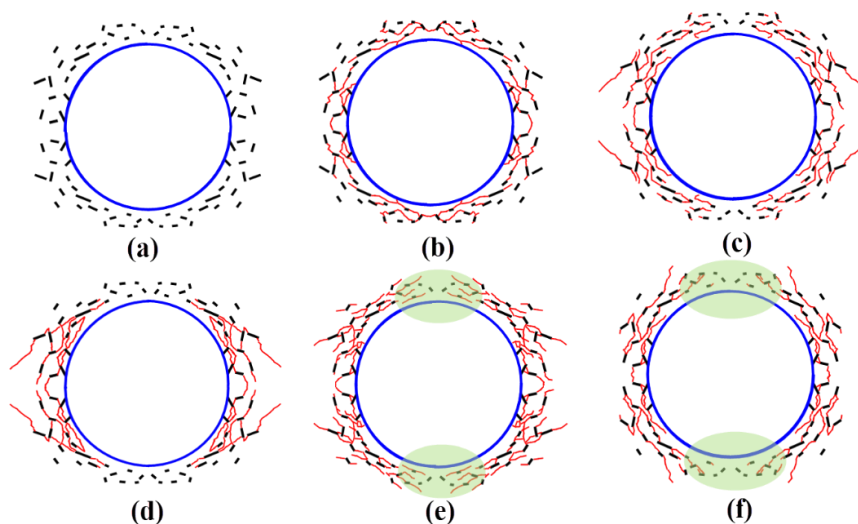
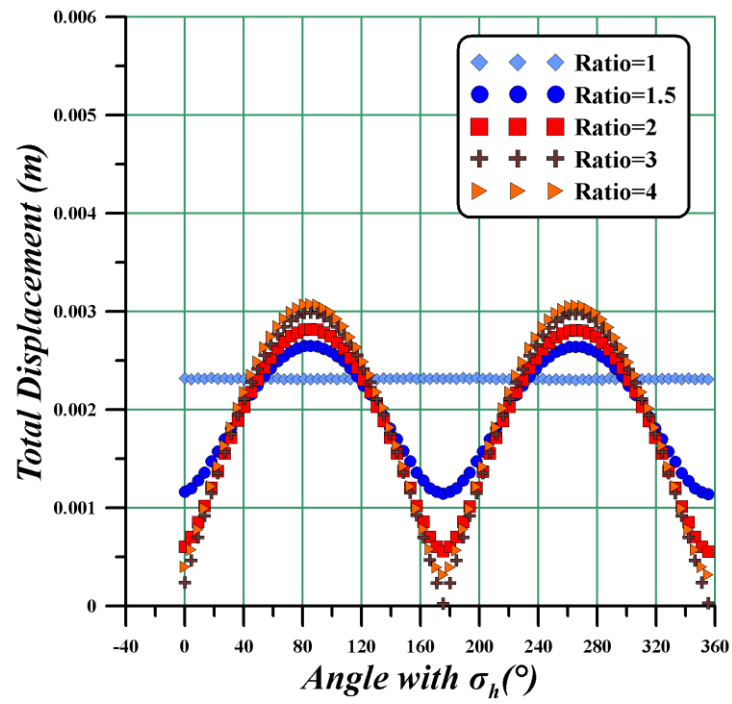
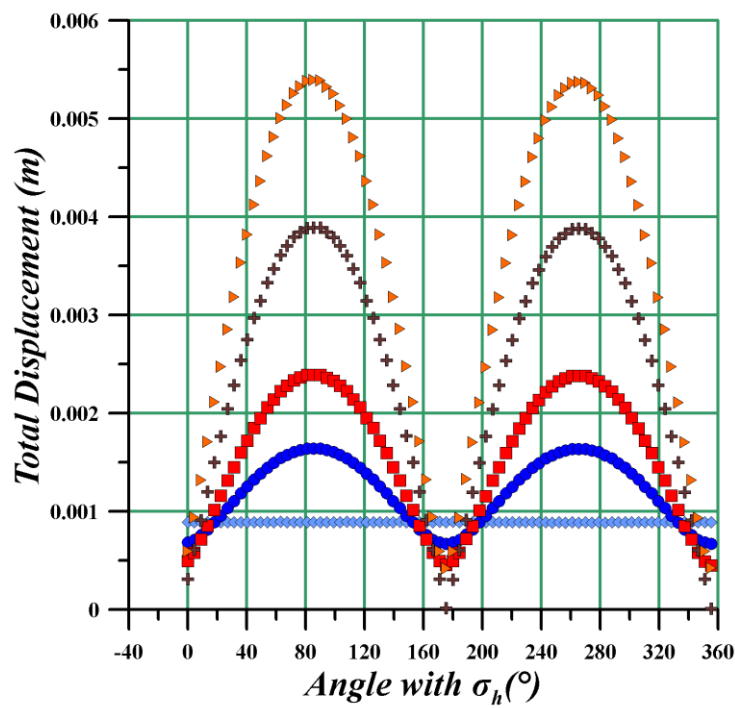


Figure 8. breakout formation for random cracks with $\sigma_H=70$ MPa a) initial model, b) $\sigma_H/\sigma_h=1$ c) $\sigma_H/\sigma_h=1.5$, d) $\sigma_H/\sigma_h=2$, e) $\sigma_H/\sigma_h=3$, f) $\sigma_H/\sigma_h=4$



(a)



(b)

Figure 9. variation of total displacements around a wellbore a) for $\sigma_H=70$ MPa b) for $\sigma_h=30$ MPa

7. Conclusions

Breakout formation in wellbores may result in instability. The formation mechanism of breakouts was studied numerically using the displacement discontinuity method. Higher-order elements were introduced and used to improve the accuracy of the numerical model in simulating cracks propagation. The numerical method was validated by several analytical solutions. Then breakout formation was studied through several numerical simulations. Numerical results showed that the ratio of normal stresses to wellbore walls (higher normal stress/lower normal stress) has a significant effect on the formation of breakouts. It was concluded that for a constant higher normal stress, higher stress ratios lead to deeper breakouts and the width of breakout does not change significantly. Also, for a

constant lower normal stress, higher stress ratios lead to wider breakouts, eventually leading to wellbore instability. In addition to that for a stress ratio of 1 (i.e. hydrostatic stress field), the formation of breakout depends on the magnitude of hydrostatic stress. If this stress is high enough in relation to the host rock UCS, then breakout formation may occur in all wellbore walls. But if the hydrostatic stress is not high enough, a minimum breakout formation may occur and the wellbore will be stable breakout-wise.

8. Acknowledgments

The authors acknowledge the financial support from Iran National Science Foundation (INSF), Tehran, and Yazd University research affairs (research project INSF-YAZD 96010905).

Appendix A.

A.1. Third-order element formulation for the DDM

A third-order displacement discontinuity (DD) element ($D_i(\zeta)$) contains four sub-elements (a1,a2,a3,a4) as shown in Fig. A.1. These sub-elements can have any arbitrary length order, but equal sub-elements facilitate the derivation of the formulation. Therefore, equal sub-elements (a1=a2=a3=a4) will be used in this study. Sub-element contains a central node. The opening displacement discontinuity D_y and sliding displacement discontinuity D_x are numerically evaluated (Fatehi Marji et al., 2009).

$$D_i(\zeta) = \sum_{j=1}^4 \varpi_j(\zeta) D_i^j, \quad i = x, y \quad (\text{A.1})$$

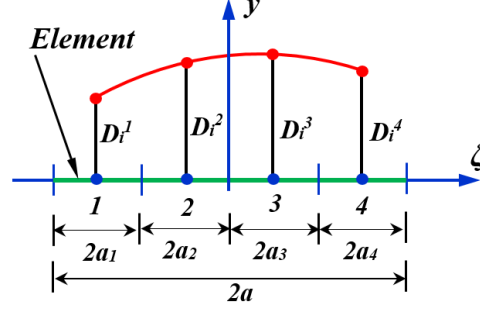


Figure A.1. Cubic collocation for a cubic element displacement discontinuity

$$\begin{aligned}
 \varpi_1(\zeta) &= (-3a_1^3 + a_1^2\zeta + 3a_1\zeta^2 - \zeta^3)/(48a_1^3), \\
 \varpi_2(\zeta) &= (9a_1^3 - 9a_1^2\zeta - a_1\zeta^2 + \zeta^3)/(16a_1^3), \\
 \varpi_3(\zeta) &= (9a_1^3 + 9a_1^2\zeta - a_1\zeta^2 - \zeta^3)/(16a_1^3), \\
 \varpi_4(\zeta) &= (-3a_1^3 - a_1^2\zeta + 3a_1\zeta^2 + \zeta^3)/(48a_1^3)
 \end{aligned} \tag{A.2}$$

Crouch derived the displacement and stress fields for a line crack in an infinite body along the x-axis in Eq. (A.3) and Eq. (A.4) respectively (Crouch, 1976):

$$\begin{aligned}
 u_x &= [2(1-\nu)f_{,y} - yf_{,xx}] + [- (1-2\nu)g_{,x} - yg_{,xy}] \\
 u_y &= [(1-2\nu)f_{,x} - yf_{,xy}] + [2(1-\nu)g_{,y} - yg_{,yy}]
 \end{aligned} \tag{A.3}$$

$$\begin{aligned}
 \sigma_{xx} &= 2G[2f_{,xy} + yf_{,xyy}] + 2G[g_{,yy} + yg_{,yyy}] \\
 \sigma_{yy} &= 2G[-yf_{,xyy}] + 2G[g_{,yy} - yg_{,yyy}] \\
 \sigma_{xy} &= 2G[2f_{,yy} + yf_{,yyy}] + 2G[-yg_{,xyy}]
 \end{aligned} \tag{A.4}$$

where G is the shear modulus, $g(x,y)$ and $f(x,y)$ are harmonic functions and $f_{,x}$, $g_{,x}$, $f_{,y}$, $g_{,y}$, etc. are the partial derivatives of $f(x,y)$ and $g(x,y)$ with respect to x-axis and y-axis. $f(x,y)$ and $g(x,y)$ for third order element case can be derived from:

$$\begin{aligned}
 f(x,y) &= \frac{-1}{4\pi(1-\nu)} \sum_{j=1}^4 D_x^j F_j(I_0, I_1, I_2, I_3) \\
 g(x,y) &= \frac{-1}{4\pi(1-\nu)} \sum_{j=1}^4 D_y^j F_j(I_0, I_1, I_2, I_3)
 \end{aligned} \tag{A.5}$$

Common function F_j in Eqs. (A.5) is defined as

$$F_j(I_0, I_1, I_2, I_3) = \int \varpi_j(\zeta) \ln \sqrt{(x-\zeta)^2 + y^2} d\zeta, \quad j = 1 \text{ to } 4 \tag{A.6}$$

where the integrals I_0 , to I_3 are defined by Eqs. (7):

$$\begin{aligned}
 I_0(x, y) &= \int_{-a}^a \ln[(x - \zeta)^2 + y^2]^{\frac{1}{2}} d\zeta \\
 &= y(\beta_1 - \beta_2) - (x - a)\ln(r_1) + (x + a)\ln(r_2) - 2a \\
 I_1(x, y) &= \int_{-a}^a \zeta \ln[(x - \zeta)^2 + y^2]^{\frac{1}{2}} d\zeta \\
 &= xy(\beta_1 - \beta_2) + 0.5(y^2 - x^2 + a^2)\ln\frac{r_1}{r_2} - ax \\
 I_2(x, y) &= \int_{-a}^a \zeta^2 \ln[(x - \zeta)^2 + y^2]^{\frac{1}{2}} d\zeta = \frac{y}{3}(3x^2 - y^2)(\beta_1 - \beta_2) + \\
 &\frac{1}{3}(3xy^2 - x^3 + a^3)\ln(r_1) - \frac{1}{3}(3xy^2 - x^3 - a^3)\ln(r_2) - \frac{2a}{3}\left(x^2 - y^2 + \frac{a^3}{3}\right) \\
 I_3(x, y) &= \int_{-a}^a \zeta^3 \ln[(x - \zeta)^2 + y^2]^{\frac{1}{2}} d\zeta = -xy(x^2 - y^2)(\beta_1 - \beta_2) \\
 &+ 0.25(3x^4 - 6x^2y^2 + 8a^2x^2 + a^4 - y^4)[\ln(r_1) - \ln(r_2)] \\
 &- 2ax(x^2 + a^2)[\ln(r_1) + \ln(r_2)] + 1.5ax^3 - 3axy^2 + 7a^3x/6
 \end{aligned} \tag{A.7}$$

and β_1 , β_2 , r_1 , and r_2 are defined as:

$$\begin{aligned}
 \beta_1 &= \operatorname{tg}^{-1}\left(\frac{y}{x - a}\right), \quad \beta_2 = \operatorname{tg}^{-1}\left(\frac{y}{x + a}\right), \\
 r_1 &= \sqrt{(x - a)^2 + y^2}, \quad \text{and } r_2 = \sqrt{(x + a)^2 + y^2}
 \end{aligned} \tag{A.8}$$

Abdollahipour et al. (Abdollahipour et al., 2015) and Fatehi-Marji et al. (Fatehi Marji et al., 2006) have completely explained the partial derivatives of I_0 to I_3 .

A.2. The special crack tip element

Special crack tip elements with four equal crack tip sub-elements were used to compensate for the lack of accuracy of the DDs values near crack ends due to singularities of the stresses and displacements at this area (Fatehi Marji et al., 2006). As shown in Fig. A.2, the variation of DDs can be formulated using a special crack tip element divided into four equal special crack tip sub-elements ($a_1 = a_2 = a_3 = a_4$).

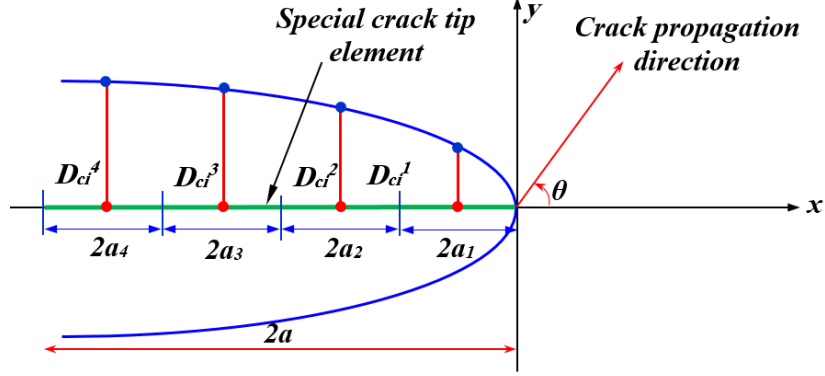


Figure A.2. Special crack tip element with four equal sub-elements

$$D_{Ci}(\zeta) = [\varpi_{C1}(\zeta)]D_{Ci}^1(a) + [\varpi_{C2}(\zeta)]D_{Ci}^2(a) + [\varpi_{C3}(\zeta)]D_{Ci}^3(a) + [\varpi_{C4}(\zeta)]D_{Ci}^4(a) \quad (A.9)$$

In which $i = x, y$ for shear and normal DDs . The special crack tip elements' shape functions $\varpi_{Ci}(\zeta)$ to $\varpi_{C4}(\zeta)$ can be obtained as (Abolfazl Abdollahipour et al., 2016):

$$\begin{aligned} \varpi_{C1}(\eta) &= 2.1336 \left(\frac{\zeta}{a_1}\right)^{\frac{1}{2}} - 1.3965 \left(\frac{\zeta}{a_1}\right)^{\frac{3}{2}} + 0.2759 \left(\frac{\zeta}{a_1}\right)^{\frac{5}{2}} - 0.0172 \left(\frac{\zeta}{a_1}\right)^{\frac{7}{2}} \\ \varpi_{C2}(\eta) &= -0.9475 \left(\frac{\zeta}{a_2}\right)^{\frac{1}{2}} + 1.2094 \left(\frac{\zeta}{a_2}\right)^{\frac{3}{2}} - 0.2787 \left(\frac{\zeta}{a_2}\right)^{\frac{5}{2}} + 0.0194 \left(\frac{\zeta}{a_2}\right)^{\frac{7}{2}} \\ \varpi_{C3}(\eta) &= 0.1908 \left(\frac{\zeta}{a_3}\right)^{\frac{1}{2}} - 0.2467 \left(\frac{\zeta}{a_3}\right)^{\frac{3}{2}} + 0.0771 \left(\frac{\zeta}{a_3}\right)^{\frac{5}{2}} - 0.0231 \left(\frac{\zeta}{a_3}\right)^{\frac{7}{2}} \\ \varpi_{C4}(\eta) &= -0.0977 \left(\frac{\zeta}{a_4}\right)^{\frac{1}{2}} + 0.150 \left(\frac{\zeta}{a_4}\right)^{\frac{3}{2}} - 0.0586 \left(\frac{\zeta}{a_4}\right)^{\frac{5}{2}} + 0.0065 \left(\frac{\zeta}{a_4}\right)^{\frac{7}{2}} \end{aligned} \quad (A.10)$$

The general potential function $F_C(x, y)$ for special crack tip elements may be found by first substituting shape functions definition (Eqs. (A.10)) into Eqs. (A.9). Then the resulted equations are substituted into displacement and stress fields equations (Eqs. (A.3) and (A.4)). Finally, following the same procedure as for the derivation of the general potential function $F_j(I_0, I_1, I_2, I_3)$ in Eq. (A.6), the general potential function $F_C(x, y)$ for a special crack tip element can be expressed as:

$$F_c(x, y) = -\frac{1}{4\pi(1-\nu)} \left\{ \left[\int_{-a}^a \varpi_{c1}(\zeta) \ln[(x-\zeta)^2 + y^2]^{0.5} d\zeta \mathcal{D}_i^1 \right] + \left[\int_{-a}^a \varpi_{c2}(\zeta) \ln[(x-\zeta)^2 + y^2]^{0.5} d\zeta \mathcal{D}_i^2 \right] + \left[\int_{-a}^a \varpi_{c3}(\zeta) \ln[(x-\zeta)^2 + y^2]^{0.5} d\zeta \mathcal{D}_i^3 \right] + \left[\int_{-a}^a \varpi_{c4}(\zeta) \ln[(x-\zeta)^2 + y^2]^{0.5} d\zeta \mathcal{D}_i^4 \right] \right\} \quad (\text{A.11})$$

The special crack tip elements' potential function $F_c(I_{Cj})$ can be written as:

$$F_c(I_{Cj}) = \int_{-a}^a \varpi_{Cj}(\zeta) \ln[(x-\zeta)^2 + y^2]^{\frac{1}{2}} d\zeta \quad (\text{A.12})$$

Then I_{Cj} integrals for four nodes of special crack tip element are derived as:

$$\begin{aligned} I_{C1}(x, y) &= \int_{-a}^a \zeta^{\frac{1}{2}} \ln[(x-\zeta)^2 + y^2]^{\frac{1}{2}} d\zeta, \\ I_{C2}(x, y) &= \int_{-a}^a \zeta^{\frac{3}{2}} \ln[(x-\zeta)^2 + y^2]^{\frac{1}{2}} d\zeta, \\ I_{C3}(x, y) &= \int_{-a}^a \zeta^{\frac{5}{2}} \ln[(x-\zeta)^2 + y^2]^{\frac{1}{2}} d\zeta, \\ I_{C4}(x, y) &= \int_{-a}^a \zeta^{\frac{7}{2}} \ln[(x-\zeta)^2 + y^2]^{\frac{1}{2}} d\zeta \end{aligned} \quad (\text{A.13})$$

The Mode I and Mode II Stress Intensity Factors (SIFs) K_I and K_{II} are required for the crack propagation simulation study. These SIFs for a crack tip element of length $2a$ can be easily and directly derived based on the LEFM (Linear Elastic Fracture Mechanics) principles (Fatehi Marji et al., 2006; Sanford, 2003) using normal (opening) and shear (sliding) displacement discontinuities (Shou and Crouch, 1995) as:

$$K_I = \frac{G}{4(1-\nu)} \left(\frac{2\pi}{a} \right)^{\frac{1}{2}} D_y(a), \quad \text{and} \quad K_{II} = \frac{G}{4(1-\nu)} \left(\frac{2\pi}{a} \right)^{\frac{1}{2}} D_x(a) \quad (\text{A.14})$$

9. References

Abdollahipour, A., 2015. Crack propagation mechanism in hydraulic fracturing procedure in oil reservoirs. University of Yazd.

Abdollahipour, A, Fatehi Marji, M., Yarahmadi Bafghi, A., Gholamnejad, J., 2016. A complete

formulation of an indirect boundary element method for poroelastic rocks. *Computers and Geotechnics* 74, 15–25. <https://doi.org/10.1016/j.compgeo.2015.12.011>

Abdollahipour, A., Fatehi Marji, M., Yarahmadi-Bafghi, A., Gholamnejad, J., Yarahmadi Bafghi, A., Gholamnejad, J., 2015. Simulating the propagation of hydraulic fractures from a circular wellbore using the Displacement Discontinuity Method. *International Journal of Rock Mechanics and Mining Sciences* 80, 281–291. <https://doi.org/10.1016/j.ijrmms.2015.10.004>

Abdollahipour, A., Fatehi Marji, M., Yarahmadi-Bafghi, A.R., 2013. A fracture mechanics concept of in-situ stress measurement by hydraulic fracturing test, in: *The 6th International Symposium on In-Situ Rock Stress*. ISRM, Japan.

Abdollahipour, Abolfazl, Marji, M.F., Bafghi, A.Y., Gholamnejad, J., 2016. On the accuracy of higher order displacement discontinuity method (HODDM) in the solution of linear elastic fracture mechanics problems. *Journal of Central South University* 23, 2941–2950. <https://doi.org/10.1007/s11771-016-3358-8>

Amadei, B., Stephansson, O., 1997. *Rock Stress and Its Measurement*. Chapman & Hall.

Baotang, S., Ove, S., Mikael, R., 2014. *Modelling rock fracturing processes*.

Castillo, D.A., Zoback, M.D., 1994. Systematic variations in stress state in the Southern San Joaquin Valley: Inferences based on well-bore data and contemporary seismicity. *American Association Petroleum Geologists Bulletin* 78, 1257–1275.

Crouch, S.L., 1976. Solution of plane elasticity problems by the displacement discontinuity method. I. Infinite body solution. *International Journal for Numerical Methods in Engineering* 10, 301–343.

Erdogan, F., Sih, G.C., 1963. On the crack extension in plates under plate loading and transverse shear. *J. Basic Eng.* 85, 519–527.

Ewy, R., Cook, N., 1990. Deformation and failure around cylindrical openings in rock. *Int J Rock Mech Min Sci Geomech Abstr* 27, 387–427.

Fatehi Marji, M., Hosseini Nasab, H., Kohsary, A.H., 2006. On the uses of special crack tip elements in numerical rock fracture mechanics. *Int. J. Solids and Structures* 43, 1669–1692. <https://doi.org/10.1016/j.ijsolstr.2005.04.042>

Fatehi Marji, M., Hosseini-Nasab, H., Morshedi, A.H., 2009. Numerical modeling of the mechanism of crack propagation in rocks under TBM disc cutters. *Mechanics of Materials and Structures* 4, 605–627.

Gerolymatou, E., 2019a. A novel tool for simulating brittle borehole breakouts. *Computers and Geotechnics* 107, 80–88. <https://doi.org/10.1016/j.compgeo.2018.11.015>

Gerolymatou, E., 2019b. A novel tool for simulating brittle borehole breakouts. *Computers and Geotechnics* 107, 80–88. <https://doi.org/10.1016/J.COMPGE0.2018.11.015>

- Gomar, M., Goodarznia, I., Shadizadeh, S.R., 2014. Transient thermo-poroelastic finite element analysis of borehole breakouts. *International Journal of Rock Mechanics and Mining Sciences* 71, 418–428. <https://doi.org/10.1016/j.ijrmms.2014.08.008>
- Guenot, A., 1989. Borehole breakouts and stress fields. *Int J Rock Mech Min Sci Geomech Abstr* 26, 185–195.
- Guo, H., Aziz, N.I., Schmitt, L.C., 1990. Linear elastic crack tip modeling by displacement discontinuity method. *Engin. Fract. Mech.* 36, 933–943.
- Haimson, B.C., Lee, M.Y., 1995. Estimating In Situ stress conditions from borehole breakouts and core diskings-experimental results in granite, in: *International Workshop on Rock Stress Measurement at Great Depth*.
- Lee, M.Y., Haimson, B.C., 1993. Laboratory study of borehole breakouts in Lac du Bonnet granite: a case of extensile failure mechanism. *Int J Rock Mech Min Sci Geomech Abstr* 30.
- Li, X., Feng, Y., El Mohtar, C.S., Gray, K.E., 2019. Transient modeling of borehole breakouts: A coupled thermo-hydro-mechanical approach. *Journal of Petroleum Science and Engineering* 172, 1014–1024. <https://doi.org/10.1016/j.petrol.2018.09.008>
- Lin, H., Kang, W.H., Oh, J., Canbulat, I., Hebblewhite, B., 2020. Numerical simulation on borehole breakout and borehole size effect using discrete element method. *International Journal of Mining Science and Technology* 30, 623–633. <https://doi.org/10.1016/J.IJMST.2020.05.019>
- Lin, W., Yeh, E.-C., Hung, J.-H., Haimson, B., Hirono, T., 2010. Localized rotation of principal stress around faults and fractures determined from borehole breakouts in hole B of the Taiwan Chelungpu-fault Drilling Project (TCDP). *Tectonophysics* 482, 82–91. <https://doi.org/10.1016/j.tecto.2009.06.020>
- Liu, H., Lin, J.S., He, J., Xie, H., 2020. A discrete element exploration of V-shaped breakout failure mechanisms in underground opening. *Underground Space (China)* 5, 281–291. <https://doi.org/10.1016/J.UNDSP.2019.05.001>
- Mansourizadeh, M., Jamshidian, M., Bazargan, P., Mohammadzadeh, O., 2016. Wellbore stability analysis and breakout pressure prediction in vertical and deviated boreholes using failure criteria – A case study. *Journal of Petroleum Science and Engineering* 145, 482–492. <https://doi.org/10.1016/j.petrol.2016.06.024>
- Martin, C., Martino, J., Dzik, E., 1994. Comparison of borehole breakouts from laboratory and field tests, in: *Proceeding on Rock Mechanics in Petroleum Engineering*. Balkema, Delft/Rotterdam, pp. 183–190.
- Newman, Jr.J.C., 1971. An Improved Method of Collocation for the Stress Analysis of Cracked Plates with Various Shaped Boundaries. NASA Technical Note, NASA TN D-6376.
- Plumb, R.A., Cox, J.W., 1987. Stress directions in eastern North America determined to 4.5 km from borehole elongation measurements. *Journal of Geophysical Research* 92, 4805–4816.

RIPI, 2016. Internal report of geomechanical tests. Tehran, Iran.

Sahara, D.P., Schoenball, M., Gerolymatou, E., Kohl, T., 2017. Analysis of borehole breakout development using continuum damage mechanics. *International Journal of Rock Mechanics and Mining Sciences* 97, 134–143. <https://doi.org/10.1016/j.ijrmms.2017.04.005>

Sanford, R.J., 2003. Principles of fracture mechanics. Prentice Hall, USA.

Shen, B., 2008. Borehole breakout and in situ stresses, in: SHIRMS 1. Perth, Australia, pp. 407–418.

Shen, B., Stephansson, O., Rinne, M., 2002. Simulation of borehole breakouts using FRACOD2D. *Oil and Gas Science and Technology* 27, 579–590.

Shou, K.J., Crouch, S.L., 1995. A higher order displacement discontinuity method for analysis of crack problems. *Int. J. Rock Mech. Min. Sci. and Geomech. Abstr.* 32, 49–55.

Tada, H., Paris, P.C., Irwin, G.R., 2000. *The Stress Analysis of Cracks Handbook*, Third. ed. ASME, New York.

Tang, Z., Kong, X., Duan, W., Gao, J., 2021. Wellbore breakout analysis and the maximum horizontal stress determination using the thermo-poroelasticity model. *Journal of Petroleum Science and Engineering* 196. <https://doi.org/10.1016/J.PETROL.2020.107674>

Vardoulakis, J., J, S., Guenot, A., 1988. Borehole instabilities as bifurcation phenomena. *Int J Rock Mech Min Sci Geomech Abstr* 25, 159–170.

Wei, Y., Feng, Y., Deng, J., Li, X., 2021. Hydro-mechanical modeling of borehole breakout in naturally fractured rocks using distinct element method. *Geomechanics for Energy and the Environment* 100287. <https://doi.org/10.1016/J.GETE.2021.100287>

Whittaker, B.N., Singh, R.N., Sun, G., 1992. *Rock fracture mechanics, principles design and applications*. Netherland.

Zang, A., Stephansson, O., 2010. *Stress field of the earth's crust*. Springer Science + Business Media, Dordrecht/Heidelberg/London/New York.

Zhang, H., Yin, S., Aadnoy, B.S., 2018. Poroelastic modeling of borehole breakouts for in-situ stress determination by finite element method. *Journal of Petroleum Science and Engineering* 162, 674–684. <https://doi.org/10.1016/j.petrol.2017.10.085>

Zoback, M.D., 2010. *Reservoir geomechanics*. Cambridge University Press.

Zoback, M.D., Mooss, D., Mastin, L., Anderson, R., 1985. Wellbore breakout and in situ stress. *J Geophys Res* 90, 5523–5530.